Bellows-type Springs for Robotics

James F. WILSON

Professor Emeritus, Duke University, 6319 Mimosa Drive, Chapel Hill, NC, USA
TEL: 919 489 3041   e-mail: jwilson@duke.edu

Norio INOU

Professor, Department of Mechanical and Control Engineering, Tokyo Institute of Technology 2-12-1,
O-okayama,Meguro-ku, Tokyo, 152-8552, Japan
TEL:+81-3-5734-2642   e-mail: inou@mech.titech.ac.jp

Bellows-type springs, or closed elastic tubes with corrugated walls, can be designed to produce three basic motions. Given a particular orientation of the corrugations, a bellows can either extend, bend laterally, or twist along its longitudinal axis when subjected to internal pressure. Bellows made of elastomeric materials such as polyurethane can be incorporated in robotic arms and in the legs of walking machines. In this research, extension was achieved by employing uniform, circumferential corrugations; bending by extending the corrugations only 180 degrees around the circumference; and twisting by orienting the corrugations at angles between 20 and 70 degrees with the longitudinal axis. The purposes of this paper are (1) to present the general quantitative results relating load, motion, and material properties for three types of bellows; and (2) to illustrate how combinations of the three can be used for a pick-and-place robotic arm and for a six-legged walking machine.

Keywords : bellows, corrugated tubes, robotic arms, spring rate ,walking machines

1. INTRODUCTION

Historically, bellows or tubes, fabricated of metal or a polymeric material with axially symmetric corrugations, have been employed in a wide variety of engineering applications, which   include protective boots covering connections in automobile suspensions, sections of motor shafts to allow for misalignment in torque transmission, and hand siphon pumps. These bellows with axially symmetric corrugations are especially useful where extension and lateral bending is required. Spring rates for such bellows were compiled by Matheny.[1] A critical survey of corrugated geometries with a critique of bellows mechanics was given by Wilson.[2] A practical type of bellows that is designed to bend when subjected to internal pressure is the Simrit finger.[3] Here, the corrugations extend only part way around the circumference. Part of this present study addresses the mechanics of such a bellows, for which applications to robotic arms have been previously documented.[4-6]   Other types of bellows for robotics include pressurized, orthotropic tubes with corrugations inclined with the long axis, and designed to twist along the longitudinal axis when pressurized.[7,8]

Reviewed herein is the mechanical behavior of extension, bending, and twisting bellows, designated as actuators when applied to robotics. New analyses, with experimental validation,   include the modeling of a bending actuator as a long slab capped by a half-ellipse of variable thickness, and a lower bound description for torsion tube orthotropy. This study concludes with two

applications of actuators in combination: a robotic arm and a walking machine.

2. BELLOWS FOR EXTENSION

Shown in Fig. 1 is a diagram of a bellows with circumferentially uniform corrugations, which is used exclusively for extension. When subjected to an internal pressure p and/or an axial load F, the axial deflection is δ. The relatively rigid interior telescoping tubes add lateral stability and serve to minimize side deflections when the bellows is subjected to lateral loading. This typical elastomeric bellows, with a Young's modulus E, has a uniform wall thickness t, a mean radius R, a wave length of $4b$, and a total length of $4bn$, where n is the number of corrugations. As suggested by Donnell,[9] the longitudinal extension δ for an applied load F can be expressed in terms of these geometric parameters and the reduced modulus E', or

$$(1) \qquad \delta = \frac{4bn}{2\pi RtE'} F$$

in which $2\pi Rt$ is the mean cross sectional area. The theories available to compute E' for various corrugation geometries such as triangular, rectangular, U-shaped, or Ω-shaped configurations were summarized by Wilson.[2]
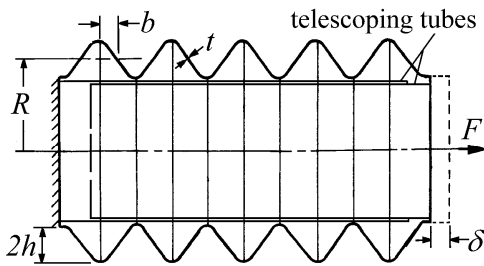
Fig. 1. An extension bellows with a telescoping tube.

2.1 Example: Use available theories to evaluate E' and the spring rates F/δ and F/p for the polyethylene siphon bellows, manufactured by Bel-Art, Ace Scientific Supply Co, USA. The siphon's dimensions are given in the insert to Fig. 2, and its Young's modulus was measured as E=199 MPa.

In the first theory, Donnell[9] assumed shallow corrugations, in which $2h/R \ll 1$ and $t/h \ll 1$, and assumed that Poisson's ratio effects were negligible (ν=0). The ratio E/E' can be calculated from the Donnell equations (2)-(4), in which $\lambda = Rt/b^2$ and $\beta = C^2/\lambda^2$.
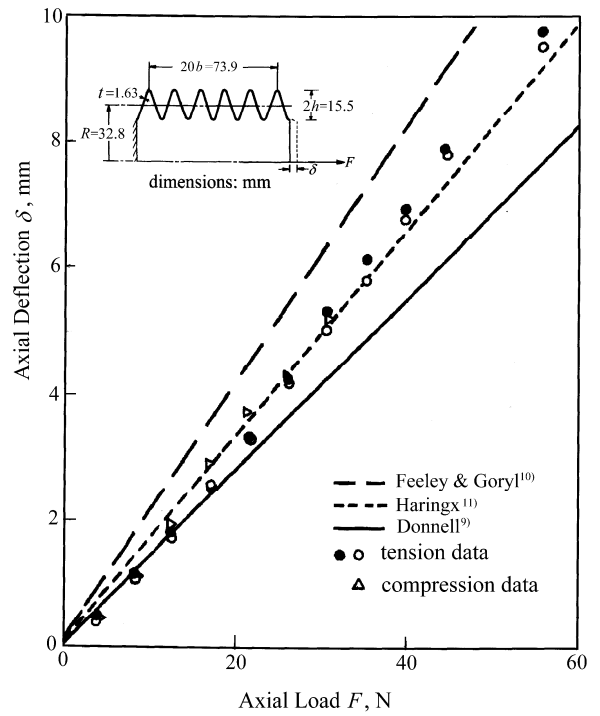
Fig. 2. Comparison of spring rates of three theories to experimental data.

$$(2) \qquad \left(\frac{E}{E'}-1\right)\frac{t}{R} = 4C\frac{h^2}{b^2}\frac{K}{\lambda}$$

$$(3) \qquad C = \sqrt{h^2/b^2 + 1}$$

$$(4) \qquad K = (1+2\beta - 0.14\beta^{1/5})^{-1}$$

The results are that E'=1.58 MPa. Using Eq. (1), the spring rate becomes F/δ=7.17 kN/m, which is the inverse slope of the solid line of Fig. 2.

In the second theory, Feeley and Goryl[10] used classical beam theory to predict the equivalent modulus for shallow triangular corrugations as

$$(5) \qquad \frac{E}{E'} = 4\frac{(h/b)^3}{(t/b)^2}$$

The results are that E'=1.05 MPa and F/δ=4.75kN/m.

In the third theory, Haringx[11] used a crimped plate theory to predict E', which can be calculated from Eqs. (6)-(8).

$$(6) \qquad \frac{E}{E'} = \frac{3(1-\nu^2)}{4(b/R)(t/R)^2}\frac{[1+(h/R)]^2}{1-\rho^2}g(\rho)$$

$$(7)\ g(\rho) = (1-\rho^2+2\rho\ln\rho)(1-\rho^2-2\rho\ln\rho)$$

$$(8) \qquad \rho = \frac{1-h/R}{1+h/R}$$

The results are that E'=1.32 MPa and F/δ=5.95 kN/m.

When E' predicted by each of these three theories is compared to the experimental value of E'=1.20 MPa (a least-squares fit), the Haringx theory of Fig. 2 shows the best agreement, with a deviation of 9.77 % from the measurement.
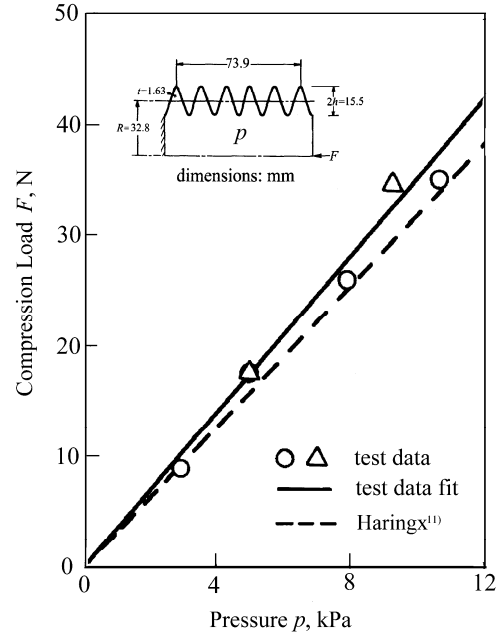
Fig. 3. Axial load required to suppress length change of an extension bellows.

Shown in Fig. 3 is a second set of experimental data on the siphon bellows. Here, the length change δ was suppressed by the compressive load F as the internal pressure p was applied. A least-squares fit of these data to a straight line gave spring rate of F/p=3.71 N/kPa. Also shown in Fig. 3 is the broken line, which is based on the Haringx theory that F/p=πR^2=3.38 N/kPa, a value that deviates by 9.7% from the measured value.

3. BELLOWS FOR BENDING

Shown in Fig. 4 is a diagram of a bending actuator, the Simrit Finger. The cross section view shows a shell consisting of a tapered bellows extending for 180 degrees around the circumference, in which the depth of the corrugations varies from a maximum at the top to zero on each flat side. This shell intersects a rectangular slab, which has dimensions of 27.7×5 mm in this example. Under internal pressure p, the bellows expands and the actuator bends about its neutral plane, which is approximately at the top of the slab section. In applications, two such actuators affixed to a common base can be used in opposition to grip an object at the tip.
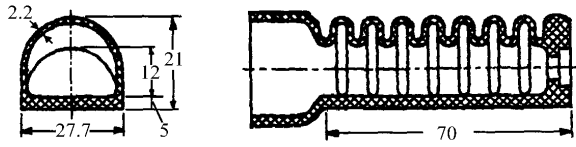
Fig.4. The Simrit Finger bending actuator, No. AU-GR1-004, US Patent No. 3981528.

3.1 Bending Experiments. Prior to formulating the general analysis of the bending behavior for this actuator, experiments were performed to determine the mechanical properties. In uniaxial tensile tests on the Simrit Finger material (polyurethane), the stress-strain behavior was found to be linear up to strains of 0.9. Young's modulus was measured as E=13.3 MPa.

The results of experiments on the actuator defined in Fig. 4, which was cantilevered at the base, are shown in Figs 5 and 6. Shown in Fig. 5 are the test data for the vertical deflection δ, measured at the bottom tip, for several values of internal pressure p. Shown in Fig. 6 are test data for the transverse tip load F that is required to maintain zero transverse tip displacement at the internal pressure p. These latter experiments indicated that the load-carrying capacity of this actuator was F=16.5 N, for which the maximum pressure was p=550 MPa. At higher pressures, the actuator was ineffective because it began to balloon as the bellows began to flatten.
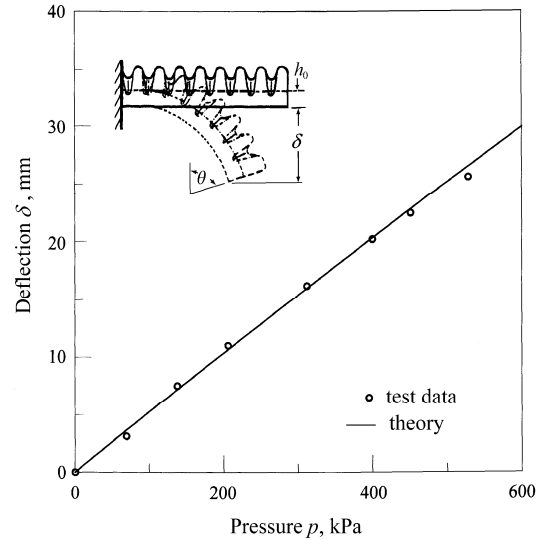
Fig. 5. Comparison of theory and test data for the Simrit Finger defined in Fig. 4.
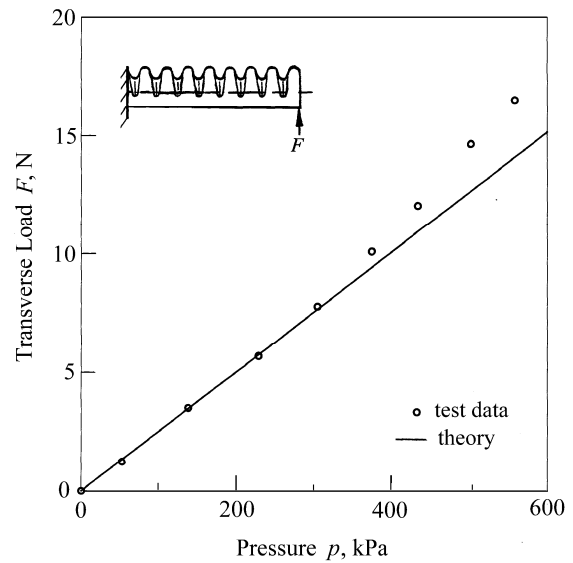
Fig. 6. Lateral load required to suppress lateral deflection of the Simrit Finger of Fig. 4.

3.2 Modeling and Analysis. The Simrit Finger is modeled as the smooth-walled tube of variable thickness, as shown in Fig. 7. Here, a rectangular slab of dimensions $2a_0 \times h_0$ is caped by a smooth shell whose thickness is the area subtended by two semi-ellipses. In terms of the (x-y) coordinate system and the ellipse dimensions defined in Fig. 7, the respective outer and inner ellipses are
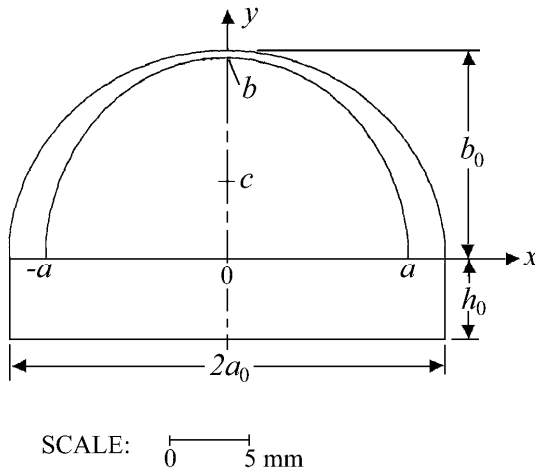
Fig. 7. Mathematical model of a Simrit Finger

$$(9) \qquad \frac{x^2}{a_0^2} + \frac{y^2}{b_0^2} = 1 \quad ; \frac{x^2}{a^2} + \frac{y^2}{b} = 1$$

For the outside ellipse, the enclosed area A_0 and the centroid of this area located at $y=c_0$ are given respectively by

$$(10) \qquad A_0 = \frac{\pi}{2} a_0 b_0 \quad ; c_0 = \frac{4b_0}{3\pi}$$

The counterpart quantities for the inner ellipse are

$$(11) \qquad A = \frac{\pi}{2} ab ; \quad c = \frac{4b}{3\pi}$$

The neutral axis for bending is chosen as the plane $y=0$. It follows that the first moment of the slab cross sectional area with respect to the neutral axis is equal to the first moment of the area subtended by the two semi-ellipses. This leads to

$$(12) \qquad 2a_0 h_0 \ h_0 / 2 = A_0 c_0 - Ac$$

With Eqs. (10) and (11), the height of the outside ellipse can be deduced from Eq. (12) as

$$(13) \qquad b_0 = \frac{3}{2a_0} \sqrt{a_0 h_0^2 + 2ab^2 / 3}$$

Here, a_0, h_0, a, and b are known design parameters, and b_0 of Eq. (13) completes the geometric definition of the mathematical model.

Needed to predict the bending deflection of the actuator under internal pressure is I_x, the second area moment of the slab-shell assembly with respect to the neutral axis. That is

$$(14) \qquad I_x = 2a_0 h_0^3 / 3 + \pi a_0 b_0^3 / 8 - \pi ab^3 / 8$$

The effective moment M at the tip of the cantilevered beam actuator of length ℓ is given by

$$(15) \qquad M = Apc = 2ab^2 p / 3$$

in which the pressure load Ap for the inner ellipse acts at its centroid $y=c$, where A and c are given by Eq. (11). From beam theory, the vertical displacement δ_0 of the neutral axis at the tip, and the rotation θ of the vertical plane at that point are given respectively in terms of M as

$$(16) \qquad \delta_0 = \frac{M\ell^2}{2EI_x} ; \quad \theta = \frac{M\ell}{EI_x}$$

With these quantities, the deflection δ at the bottom tip (see the insert of Fig. 5) can be computed in terms of M or p from Eq. (15). Thus

$$(17) \qquad \delta = \delta_0 - h_0 (1 - \cos \theta)$$

The transverse load-carrying capacity of the actuator can be computed as follows. In the absence of internal pressure, the transverse load F applied at the tip

(see the insert of Fig. 6) results in a transverse tip deflection of

$$(18) \qquad \delta_F = \frac{F\ell^3}{3EI_x}$$

If sufficient internal pressure is applied so that $\delta_0 = \delta_F$, the lateral deflection is suppressed. It follows from Eqs. (15), (16) and (18) that the external load for this condition, depicted in the insert to Fig. 6, is

$$(19) \qquad F = \frac{ab^2}{\ell} p$$

These theoretical results are now compared to the experimental data of Figs. 5 and 6. That is, using the numerical values of a_0, h_0, a, b, ℓ and E listed in the caption of Fig. 7, numerical values of b_0, M, δ_0, θ, and δ were computed from Eqs. (13)-(17) as a function of pressure p. The results of these calculations are depicted as the solid curve in Fig. 5, which is in excellent agreement with the test data. The results of the calculations for the load-carrying capacity F as a linear function pressure, Eq. (19), are shown in Fig. 6. These results compare favorably with the measurements up to pressures of about 300 kPa. At higher pressures, the theory underpredicts the value of F due to ballooning and the subsequent loss of actuator resistance to bending

.

4. BELLOWS FOR TORSION

4.1 The Experimental Model. Shown in Fig. 8 is a design of an experimental torsion bellows actuator, which twists about the longitudinal axis at elevated internal pressures. Twist occurs because the bellows corrugations are inclined at angle θ_0 with the longitudinal axis. The casting die for this actuator was constructed of two sets of concentric brass discs, each about 4 mm thick, and stacked concentrically to a height of 83 mm. The discs were shaped so that the space between the two stacks followed the dimensions

of section A-A of Fig. 8. In the die, the adjacent discs were offset by about one degree of rotation so that the stack formed a helix of $\theta_0 = 70$ degrees. The experimental actuator was cast of type A150 black rubber. Based on standard tensile tests of this same material, Young's modulus was measured as $E = 16.1$ MPa, a value obtained after several cyclical loadings of the tensile specimen.

dimensions: mm   SECT. A-A
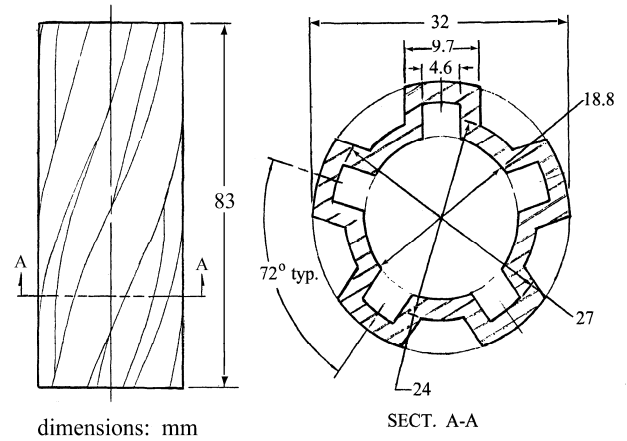
Fig. 8. A torsion actuator design, for which the helix angle is $\theta_0 = 70$ degrees.

4.2 Mathematical Model. The torsion actuator was modeled as the smooth, thin-walled, orthotropic cylinder defined in Fig. 9. The cylinder has a height ℓ, a mean
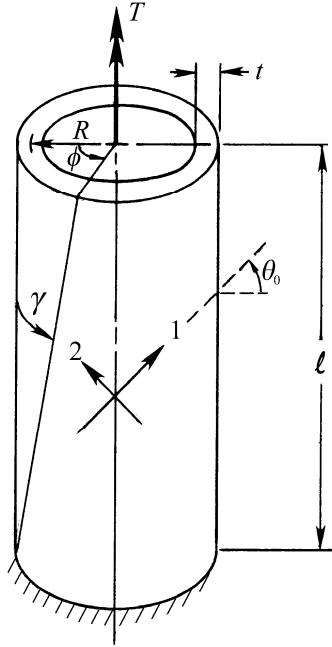
Fig, 9. A smooth-walled orthotropic cylinder model representing a torsion actuator.

radius R, and a uniform thickness t. The orthogonal directions are (1,2) , for which the values of Young's modulus are E and E' , respectively. The ridges and valleys of the corrugations follow along the 1-direction, inclined at angle θ_0. Based on the theory of elasticity, Wilson and Orgill[7] derived three nondimensional system parameters to characterize the relationships among the cylinder's dimensions R, ℓ, and t, the moduli E and E' , the applied torque T, the internal pressure p, and the angle of rotation ϕ. Those three parameters, Π_1, Π_2, and Π_3 are defined in the left column of Table 1.

Typical theoretical results are shown in Figs. 10 and 11 for Π_1 and Π_2, respectively, plotted as a function of the helix angle and E/E'. The curves of Fig. 10, for instance, show that regardless of the value of E/E', the peak rotation for an unrestrained cylinder at a given pressure occurs for $\theta_0 = 53$ degrees. However, the curves of Fig. 11, the case of complete suppression of rotation achieved by applying sufficient torque to the pressurized cylinder, show the strong dependency of the

peak torque on both θ_0 and E/E'. For instance, if a high torque actuator is required, given that $E/E' = 20$, then $\theta_0 = 75$ degrees produces the peak torque. The theoretical results for Π_3, the torque-rotation behavior for a non-pressurized cylinder, are given by Wilson and Orgill[7] in Fig. 4 of their study.
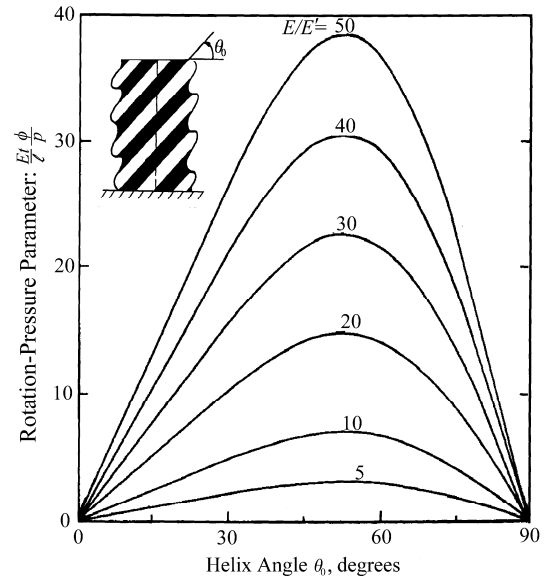
Fig. 10. Predicted behavior of the rotation-internal pressure ratio for an unrestrained, orthotropic cylinder.
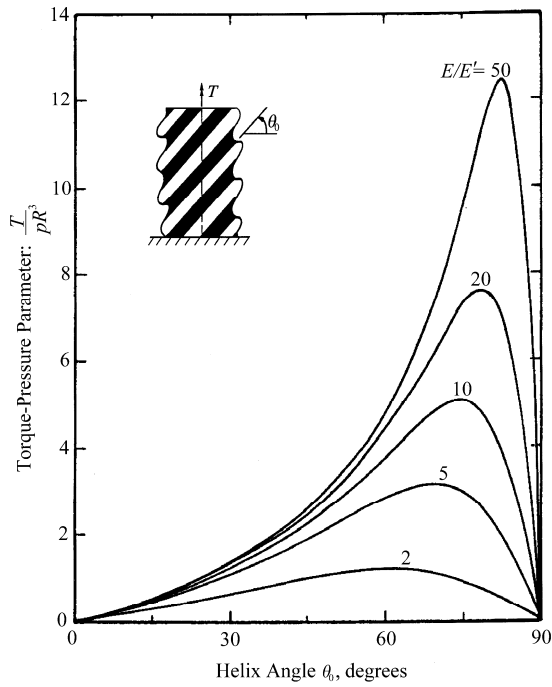
Fig. 11. Predicted behavior of the applied torque-internal pressure ratio for an orthotropic cylinder with rotation suppressed.
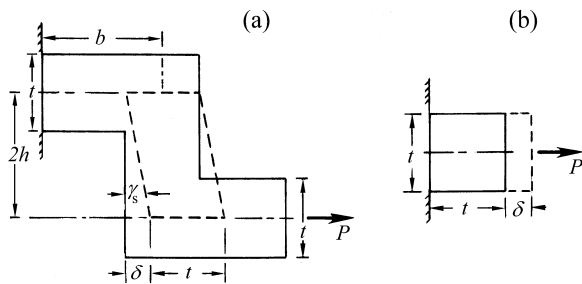
Fig. 12. (a) Rectangular model of a torque actuator's half-corrugation of modulus E; and (b) the equivalent uniform model of modulus E'.

Unlike the case of the extension bellows, there are at present no refined, closed form theories that predict E/E'

for torsion actuators. However, a reasonable lower bound for this ratio can be deduced by using the strength-of-materials approach and the simple shear model for the rectangular, half-corrugation model shown in Fig. 12(a). With internal pressure, a force component P per unit height acts in the 2-direction (see

Fig. 9. The uniform block of dimensions $t \times 2h$, outlined by the broken lines, undergoes a shear deformation γ_s due to a shear stress P/t. From linear theory, $P/t = \gamma_s E/3$, in which $E/3$ is the shear modulus. Thus, due to this shear, the block displacement in the 2-direction becomes

$$(20) \qquad \delta_s = 2h\gamma_s = 2h\frac{3P}{tE}$$

Define the equivalent modulus E' for the block shown in Fig. 12(b), a uniform block of dimensions $t \times t$. Under P, the uniform tensile load per unit height, the block extension is given by

$$(21) \qquad \delta_u = \frac{Pt}{tE'}$$

When δ_s is equated to δ_u, the modulus ratio becomes

$$(22) \qquad \frac{E}{E'} = 6\frac{h}{t}$$

Equation (22) represents a lower bound on E/E' because the displacement defined for the corrugation was too low–it did not include bending deformations. Such a lower bound is helpful in torsion actuator designs with steep helix angles and with corrugation heights $2h$ of the same order of magnitude as the thickness t. Since these two features characterize the design example of Fig. 8, then Eq. (22) applies and $E/E'=6(2.03)/2.54=4.8$. The following experiments show that this modulus ratio does represent a lower bound value for this torsion actuator.

Table 1   Parameters for the torsion actuator model of Fig. 9: E=16.1 MPa, ν=0.5, t=2.54 mm, h=0.03 mm, R=12.7 mm, ℓ=82.6 mm, and θ_0=70 degrees.

Definitions	Measurements	Π	$\dfrac{E}{E'}$
$\Pi_1 = \dfrac{Et}{\ell}\left(\dfrac{\phi}{p}\right)$	$\dfrac{\phi}{p} = 7.38$ rad/MPa (condition: T=0)	3.60	7.1
$\Pi_2 = \dfrac{1}{R^3}\left(\dfrac{T}{p}\right)$	$\dfrac{T}{p} = 6.90$ N·m/MPa (condition: ϕ=0)	3.37	5.5
$\Pi_3 = \dfrac{tER^3}{\ell}\left(\dfrac{\phi}{T}\right)$	$\dfrac{\phi}{T} = 0.966$ rad/N·m (condition: p=0)	0.98	8.5

4.3 Experimental Results. Consider the three nondimensional system parameters defined in Table 1. For each parameter, the quantity in parentheses was measured for the torsion actuator design of Fig. 8.

In the first set of experiments, the ϕ vs p data for the unrestrained actuator were found to be linear up to (ϕ,p) =(0.38 rad, 55 kPa), at which point the actuator began to balloon. A least-squares linear fit of such data (18 sets) gave ϕ/p=7.28 rad/Mpa, for which Π_1 =3.60. Interpolation of the curves in Fig. 10 then gave and E/E'=7.1.

In the second set of experiments, the T vs p data for the actuator (restrained from rotation by torque T) were found to be linear up to (T,p) =(0.426 N·m, 62.0 kPa), at which point the actuator began to loose its basic shape. A least-squares linear fit gave T/p=6.90 N·m/Mpa, for which Π_2 =3.37. Interpolation of the curves in Fig. 11 then gave and E/E'=5.5.

In the third set of experiments, the ϕ vs T data for the unpressurized actuator were found to be linear up to (ϕ,T)=(0.209 rad, 0.226 N·m). A least-squares linear fit gave ϕ/T=0.966 rad/N·m, for which Π_3 =0.980. Interpolation of the curves in Fig. 4 of Wilson and Orgill[13] then gave and E/E'=8.5.

The results of these three types of experiments, which are summarized in Table 1, gave an average modulus ratio of 7.0±1.5. Such results serve to validate the orthotropic cylinder as a reliable model for a torsion actuator, and justify the use of Eq. (22) as a reasonable lower bound predictor of E/E'.

5. BELLOWS FOR ROBOTIC ARMS

Shown in Fig. 13 is a string of Simrit Finger bending actuators forming a manipulator arm, with a gripper at the tip. The three types of actuators, labeled 3,4 and 5 are 64, 92, and 130 mm long, respectively. At the fixed end, the largest actuators sustain the largest arm moments when the pressurized arm with a payload at the gripper is displaced from the vertical equilibrium position. The total length of the arm and gripper, including the connections, was 65 cm. The actuators are oriented so that out-of-plane motion can be achieved during object manipulation. Each arm actuator has its own air supply line, which is connected to a control module. The two opposing actuators of the gripper have a common air supply. Detailed descriptions of the electronic interfaces between the control module and the microcomputer that allowed for software control of the actuator pressure-time histories, are given by Wilson et al.[12]
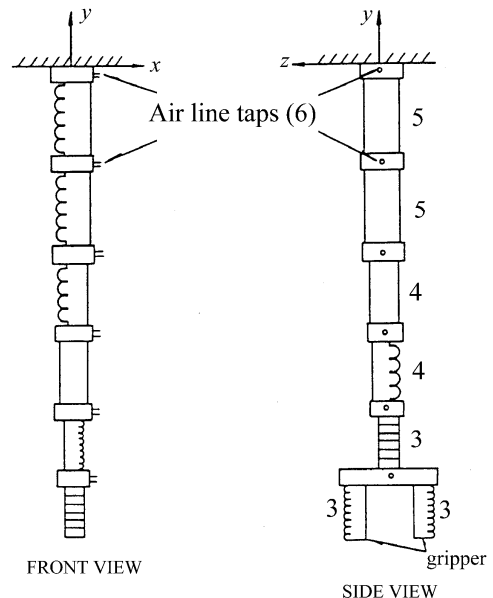
Fig. 13. A string of bending bellows forming a robotic arm.

A typical experiment for a pick-and-place maneuver is shown in Fig. 14, which depicts tracings of a photograph taken with stroboscopic light.[13] At A, the gripper is pressurized and grasps a wood block. The arm actuators are selectively pressurized and depressurized to lift the block to avoid a collision with the lower shelf. Proceeding to points B,C,D,E, the block is then deposited on the upper shelf at F, and the arm returns to its near-vertical position. The whole maneuver was achieved in five seconds.

It was found that pulsing the pressure gave the smoothest arm motion. In repeated experiments for this maneuver, it was also found that the deviation of the placement point F from its target position on the upper shelf, was no more than nine percent. It was concluded that this open-loop control method is quite robust and practical in applications where high placement accuracy is not a priority.
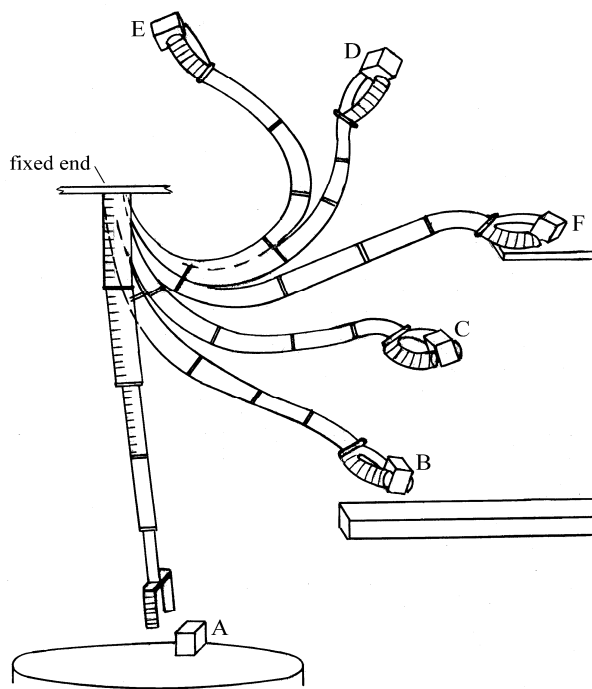
Fig. 14. Tracings of a stroboscopic photograph showing a typical maneuver of a robotic arm.

6. BELLOWS FOR WALKING ROBOTS

Shown in Fig. 15 is a six-legged walking machine, in which each leg has two types of bellows actuators.

The total length of each leg is 225 mm. Each leg is attached to a horizontal beam structure, which is 360 mm long and 190 mm wide. The upper leg segment is the Simrit Finger shown in Fig. 4. The lower segment is a neoprene extension bellows, to which was added an inner telescoping tube for lateral stability. An inner coaxial tension spring extends end-to-end so that the bellows are fully compressed when unpressurized. To suppress ballooning, this leg segment is contained in a tube of metal wire mesh.
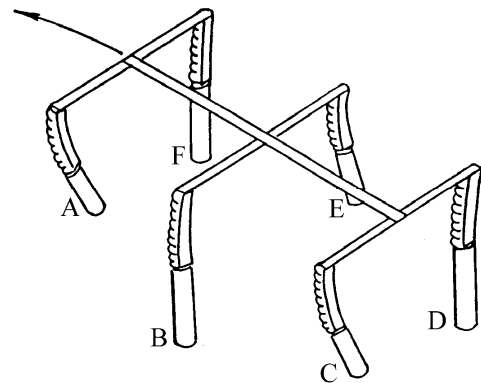
Fig. 15. Each leg of this six-legged walking machine has a bending bellows and an extension bellows.

Two forward walking gaits were investigated: fast and slow. For the fast gait, the two sets of legs, designated A-E-C and F-B-D in Fig. 15, had synchronized motions with a 180 degree phase difference. One of the two leg sets supported the robot's body while the other set stroked forward. For forward motion control, only four pressurized tubes were needed. The fast forward speed was about 20 m/s.

For the slow forward gait, the three pairs of legs, designated B-F, C-E, and A-D, were driven at a 120 degree phase difference. Four legs were always in the power stroke mode and two legs were in the reversion mode. To control the sequence, six pressurized tubes were needed. The robot was more stable at the slow walking gait of 10 m/s than at the fast forward gait of 20 m/s.

Steering, a derivative form of the fast forward gait, was realized by adding a slower than ordinary power

stroke to an active leg set. For instance, to steer the robot to the left, a slow power stroke was imposed on leg B of set F-B-D, during which slow power strokes were imposed alternatively on legs A and C of set A-E-C. Such stroke sequences produced a velocity difference between the right and left sides of the robot, and hence a steering motion. Typically, the steering radius was 1200 mm, in which the angular velocity was about one degree per second.

Pure rotation, the special case of zero steering radius, was realized by changing the same legs that exhibited slow power strokes in steering to legs that were motionless, and thus acted as pivots. With just two such legs in the static pressure state, the flexibility of the leg elements allowed for body rotation, which was typically about 0.3 degrees per second.

REFERENCES

1) J. D. Matheny, Machine Design 3, 137 (1962).

2) J. F. Wilson, Int. .J. Mech. Sci. 26, 593 (1984).

3) U.S. Patent No. 3981528 (1976).

4) J. M. Snyder and J. F. Wilson, J. Appl. Mech. 57, 203 (1990).

5) J. F. Wilson and U. Mahajan, J. Mechanisms Transmissions Automation in Design 111, 230 (1989),

6) J. F. Wilson and J. M. Snyder, J. Appl. Mech. 55, 845 (1989).

7) J. F. Wilson and G. Orgill, J. Appl. Mech. 53, 249 (1986).

8) J. F. Wilson and G. Orgill, J. Appl. Mech. 53, 257 (1986).

9) L. H. Donnell, J. Appl. Mech. APM-54-7,69, (1932).

10) F. J. Feeley and W. M. Goryl 17, 135 (1950).

11) J. A. Haringx, Phillips Res Rept. 7, 189 (1952).

12) J. F. Wilson, D. Li, Z. Chen, and R. George, *Robots and Biological Systems: Towards a New Bionics?,* edited by P. Dario, G. Sandini and P. Aebischer (Springer-Verlag, Berlin, 1993) pp. 475-494.

13) A. Benson, Sci. American 256, 73 (1987).